Check for updates

*Small*

NANO · MICRO small
www.small-journal.com

RESEARCH ARTICLE OPEN ACCESS

# Accessing Both Electrochemical SEIRA and SERS With Highly Sensitive Metamaterials for Enhanced Molecular Identification

Nicolas Spiesshofer[1] | Tabitha Jones[1] | Sarah May Sibug-Torres[1] | Zoltan Sztranyovszky[2] | Caleb Todd[1] | Shijie Zhu[1] | Yeeun Roh[1] | Rakesh Arul[1] | Alexander Squires[3] | Ivana Qianqi Lin[4] | Angela Demetriadou[2] | David O. Scanlon[3] | Viv Lindo[5] | Jeremy J. Baumberg[1]

[1]NanoPhotonics Centre, Cavendish Laboratory, Department of Physics, University of Cambridge, Cambridge, UK | [2]School of Physics and Astronomy, University of Birmingham, Birmingham, UK | [3]School of Chemistry, University of Birmingham, Birmingham, UK | [4]Hybrid Materials for Opto-Electronics Group, Department of Molecules and Materials, MESA+ Institute for Nanotechnology and Center for Brain-Inspired Nano Systems, Faculty of Science and Technology, University of Twente, Enschede, the Netherlands | [5]Analytical Sciences, BioPharmaceuticals Development, R&D, AstraZeneca, Cambridge, UK

**Correspondence:** Jeremy J. Baumberg (jjb12@cam.ac.uk)

**Received:** 4 June 2026 | **Revised:** 21 September 2026 | **Accepted:** 5 October 2026

**Keywords:** metamaterial | mid-infrared | plasmonics | SEIRA | sensing | SERS | spectro-electrochemistry

## ABSTRACT

Surface-enhanced IR absorption (SEIRA) and surface-enhanced Raman spectroscopy (SERS) are complementary techniques that allow for highly sensitive chemical fingerprinting. Non-invasive optical sensing would be significantly improved by a robust implementation of a reusable substrate that combines these techniques. Here, we present an electrochemically cleanable metamaterial that enables flow-compatible real-time SEIRA and SERS. This metamaterial facilitates the study of surface-adsorbed species and diffusion layers, elicits spectral shifts from changes in nanogap refractive index of 1400 nm/RIU, and delivers sensitive analyte detection. Combining SERS and SEIRA clarifies molecular (electro)chemical transformations and tracks changes in selection rules and symmetry breaking at the analyte-electrode interface. This development in enhanced multimodal spectro-electrochemistry is suited for multiple domains, including understanding charge transport mechanisms and interfacial dynamics at electrodes, and is capable of real-time flow monitoring for a wide range of molecular processes.

## 1 | Introduction

Surface-enhanced IR absorption (SEIRA) and surface-enhanced Raman spectroscopy (SERS) use plasmonic substrates that enhance incoming radiation to probe analytes at lower concentrations. They thus overcome challenges of traditional spectroscopic techniques such as strong water absorption of infrared light, limited sensitivity, and background interference. They enable continuous tracking of analyte molecular vibrational resonances and redox states, providing real-time insight into electrochemical reaction pathways, products, and interfacial reactions at electrode surfaces [1]. Using SERS and SEIRA in conjunction yields deep mechanistic insights into a wide range of molecular sensing applications [2–4] and electrochemical processes, such as the mechanism of the carbon dioxide reduction reaction ($CO_2RR$) [5, 6].

Spectro-electrochemistry allows for monitoring electrochemical reactions, with electrochemical SEIRA and SERS (EC-SEIRA, EC-SERS) having applications in fields ranging from catalysis to battery research [1, 7]. The adsorption of carbon monoxide [8–10], reduction of oxygen [11, 12], carbon dioxide [5, 6] and nitrogen [13], as well as molecular catalysts [14] have been studied with IR and SEIRA spectro-electrochemistry. Additionally, measuring

This is an open access article under the terms of the Creative Commons Attribution License, which permits use, distribution and reproduction in any medium, provided the original work is properly cited.
© 2026 The Author(s). *Small* published by Wiley-VCH GmbH

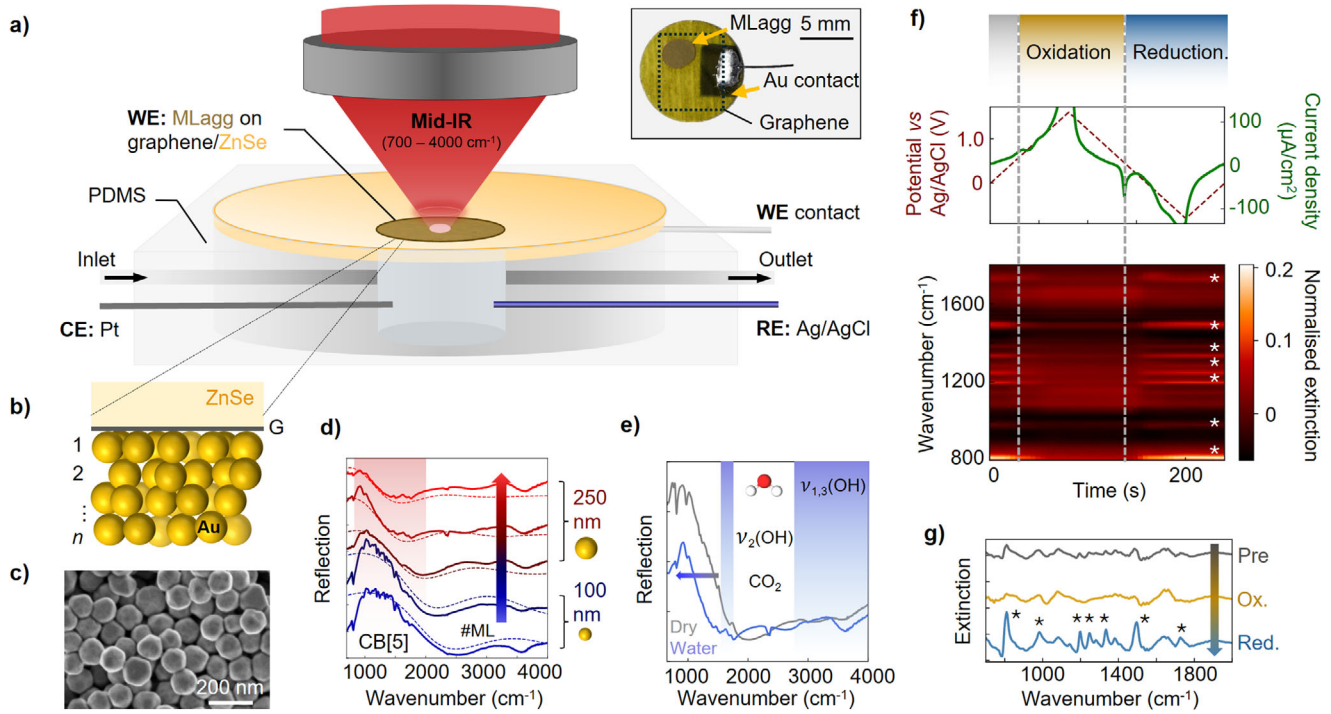



**FIGURE 1** | (a) EC-SEIRA flow cell, showing flow setup with inlet, outlet, and sample well. Labelled working electrode (WE), reference electrode (RE) and counter-electrode (CE), with inset showing an image of the device, graphene region dashed. (b) Layers of MLagg below graphene (G) and ZnSe. (c) SEM of MLagg on graphene/ZnSe. (d) Tuning of mid-IR resonance of MLaggs in water for different layer numbers and nanoparticle size, with transfer matrix fits (dashed). (e) Dry vs. aqueous mid-IR reflectivity with water absorption bands highlighted. Arrow shows red-shift of the resonance. (f) SEIRA spectro-electrochemistry showing regeneration of substrate and cyclic voltammetry. Oxidation and reduction sections labelled. (g) In situ electrochemical cleaning of MLagg (Pre = before cleaning), showing stronger molecular vibrational resonances of CB[5] after ReSERS (Red.). In (f),(g), asterisks (*) label CB[5] vibrations.

vibrational Stark shifts (changes in vibrational frequencies due to an externally applied potential) enables the study of local pH, the electrical double layer (EDL), and gas adsorption in EC-SERS [8, 15, 16].

Combining SEIRA and SERS is crucial to obtain a complete set of molecular fingerprints as they are sensitive to different subsets of vibrational modes. However, creating electrochemical substrates combining resonant SEIRA with SERS has been challenging. Nanoantennae and nanoslit arrays can support spectro-electrochemical measurements with resonant SEIRA [9], enabling enhancement factors up to $10^6$. However, top-down lithography methods typically fail to create reproduceable few-nanometer gaps that support high-enhancement SERS. By contrast, some SERS substrates based on chemical self-assembly or electrochemical roughening can also support non-resonant SEIRA, but only give 100–1000x signal enhancement of adsorbed species [17]. Such substrates also tend to be less robust, less reproducible, and less stable at useful potentials [18]. Self-assembled substrates combining resonant SEIRA and SERS based on metallic nanoparticles [17, 19, 20] open up the use of readily-fabricated metamaterial films for in situ low-concentration chemical sensing.

A common issue with all the above studies is degradation, which occurs due to irreversible binding of analytes (such as gases and biomolecules) to the SERS/SEIRA substrate, affecting any subsequent measurements with the same substrate. 'ReSERS' [21] is a recently developed method that uses electrochemical oxidation of gold nanoparticles to repeatedly strip off analytes, maintaining low variability (<5%) across samples over many use cycles. By contrast, in situ electrochemical regeneration for SEIRA has not yet been achieved, due to the lack of suitable substrates. Initial work to develop reusable SEIRA sensors includes the use of regenerated liquid gallium [22] and protective polymer layers [23] for targeted applications. However, this remains an underdeveloped area within the field.

Here, we report an EC-SEIRA/SERS substrate that uses multilayer aggregates (MLaggs) of precision-spaced AuNPs supported on graphene-capped ZnSe for electrochemical measurements in solution at trace concentrations. We show that this substrate is reusable via electrochemical oxidation/reduction, thereby removing all analytes. We test this substrate by monitoring the model redox reaction of ferrocyanide, detecting both SEIRA and SERS. This ferrocyanide/ferricyanide redox couple has distinct IR and Raman peaks, which change depending on the oxidation state of the analyte [18, 24]. We find that monitoring the redox couple via both SEIRA and SERS on the same device architecture yields insights into the diffusion-limited behavior within the tortuous metamaterial and highlights symmetry breaking of the molecule at electrodes. The resulting emergence of simultaneously IR- and Raman-active species bound at metal surfaces has implications for plasmon-driven chemistry and catalysis, for example, in improving hot electron transfer [25].



16136829, 0, Downloaded from https://onlinelibrary.wiley.com/doi/10.1002/smll.76283 by JEREMY BAUMBERG - Cambridge University Library , Wiley Online Library on [16/10/2026]. See the Terms and Conditions (https://onlinelibrary.wiley.com/terms-and-conditions) on Wiley Online Library for rules of use; OA articles are governed by the applicable Creative Commons License

## 2 | Results and Discussion

### 2.1 | MLaggs on Graphene as Reusable EC-SEIRA Sensors

The assembly of gold nanoparticles into close-packed aggregate films (MLaggs) as well as their stacking to obtain tuneable resonances has been shown in previous work [17, 19]. These precision-spaced 100 nm AuNPs separated by 0.9±0.05 nm gaps defined by cucurbit[5]uril (CB [5]) spacer molecules, form a random close-packed metamaterial (Figure 1a–c). These MLaggs give strong resonances with intense optical hotspots inside each nanogap. Sequential deposition of up to 10 stacked MLaggs (10MLs) red-shifts the resonance into the molecular fingerprint mid-IR spectral region, and can be further red-shifted using larger 250 nm diameter AuNPs (Figure 1d). The SEIRA vibrational resonances of CB[5] exhibit clear Fano lineshapes that tune in amplitude and phase with the number of MLagg layers and AuNP size, in contrast to previous non-resonant EC-SEIRA substrates [8, 11, 14]. Their strong IR enhancement allows detection of a range of small molecules at low concentration in solution, such as pharmaceutical compounds (amantadine) or DNA bases (Figure S1).

To introduce electrochemical control with back-side NIR/MIR access and thus develop EC-SEIRA and EC-SERS, we deposit AuNP MLaggs on the IR-transparent conductive monolayer graphene (2D/G ratio > 2, Figures S2 and S3), which is coated onto ZnSe and connected via Au contacts and Pt wiring (Figure 1a). The light absorption of this conducting support is identical to ZnSe since graphene absorbs minimally in the visible and mid-IR spectral region [18]. The use of ZnSe is advantageous as its transparency from ~ 600 nm to the far-IR avoids masking molecular vibrations that are obscured with other substrates such as $SiO_2$. Crucially it also allows NIR light to penetrate, thus accessing the MLagg plasmonic resonances that give intense SERS. As shown below, the MLaggs electrically contact the graphene layer, providing an EC-metamaterial on a fully transparent substrate. These devices are used in a compact microfluidic cell, which integrates flow channels and electrochemical electrodes and fits underneath an IR/Raman microscope (Figure 1a).

The deposition of MLaggs on graphene (G/ZnSe) leads to resonances in the mid-IR, which for optimal sensing should be tuned to the desired MIR vibrations. We have shown that since the wavelength (5–10 μm) is much larger than the NP size and spacing, the MIR optical field distribution can be understood by treating the MLagg metamaterial as a high-refractive-index effective medium [26] and applying transfer matrix methods (adapted from [17]). This gives distinct peaks in reflectance (Figure 1d) and absorption. These match the reflectance spectra closely and can be used to predict the electric field envelope in the metamaterial, which has a maximum at the ZnSe/metamaterial interface and an antinode at the metamaterial-air/water interface (Figure S4). Conversely, the field envelope in the near-infrared ($\lambda$ = 785 nm) exponentially decays over the depth of the metamaterial, with most of the field only present in the top MLagg layer (Figure S5). Within this field envelope, the light is further highly concentrated within the plasmonic hotspots, with the location of hotspots probed depending on the resonance tuning.

Crucially, we now find that the water absorption bands do not obscure the CB[5] vibrational resonances or those of analytes, which is essential for sensing in aqueous conditions. Specifically, the O-H bending mode ~1600 $cm^{-1}$ is only double the 1750 $cm^{-1}$ carbonyl CB[5] absorption (Figure 1e), showing that these substrates are suitable for IR flow sensing, which is replicated with other solvents (Figure S6) in static conditions.

The electrochemical properties of the G/ZnSe support (without MLaggs) show excellent conductivity and stability over a wide voltage window (at least $-0.8\ V < V < +1.5\ V$ vs. Ag/AgCl, Figure S7, larger anodic potentials possible [27]). To demonstrate the reusability of the substrate, we remove surface-bound species by sweeping the applied potential over the gold oxidation potential, followed by a gap 'rescaffolding' step via gold reduction in the presence of CB[5]. Cyclic voltammetry (CV) in 1 M pH 7 potassium phosphate buffer (KPB) and 1 mM CB[5] with 5 $mVs^{-1}$ scan rate shows characteristic anodic and cathodic current peaks corresponding to the oxidation and reduction of Au [21], indicating that the MLagg surfaces are oxidized and reduced (Figure 1f). Oxidizing potentials (>+1.0 V) lead to a clear decrease in the amplitude of all CB[5] vibrational resonances (Figure 1g), indicating desorption of surface-bound species as the MLagg hotspot becomes plugged by gold oxide [21]. Reducing potentials (<+0.3 V) in CB[5] solution have the opposite effect, with all CB[5] vibrational resonances restored. By oxidizing and reducing the MLagg after initial fabrication, it is pre-cleaned (as previously demonstrated for SERS and clearly shown in XPS from the decrease in N(1s) signal of adsorbed organics using this protocol [21, 28]) and thus primed for sensing (Figure 1g). After this pre-cleaning, the SEIRA signal of CB[5] has now doubled due to removal of other surface-bound species (such as citrate surfactant as evidenced by SERS [21]), enhancing Au surface coverage by CB[5]. Adsorbed analytes can also be subsequently removed from the nanogaps, though we note that some trace adsorbed analytes below the sensor detection limit may persist [21]. Electrochemical cleaning in SEIRA thus regenerates the surface to its original state and allows continuous real-time sensing (as shown for ferricyanide, Figure S8).

### 2.2 | Electrochemical Regeneration Effects on Molecular Vibrations and MIR Resonances

To assess the stability and reusability of the substrate over time, we perform multiple oxidation and reduction sweeps, demonstrating the practical use for continuous monitoring. We monotonically cycle the potential to oxidize and rescaffold the MLagg five times in 1 M, pH 7 KPB and 1 mM CB[5] at 5 $mVs^{-1}$ with respect to Ag/AgCl reference and Pt wire counter-electrode, while observing changes in molecular vibrations coupled to the MIR reflectance mode. We find that cycling between Au oxidation and reduction does not adversely affect the MLagg resonance or the electrode surface, with the metamaterial resonance staying stable over multiple cycles and providing repeatable molecular vibrational signals (Figure 2a,b).



16136829, 0, Downloaded from https://onlinelibrary.wiley.com/doi/10.1002/smll.76283 by JEREMY BAUMBERG - Cambridge University Library , Wiley Online Library on [16/10/2026]. See the Terms and Conditions (https://onlinelibrary.wiley.com/terms-and-conditions) on Wiley Online Library for rules of use; OA articles are governed by the applicable Creative Commons License

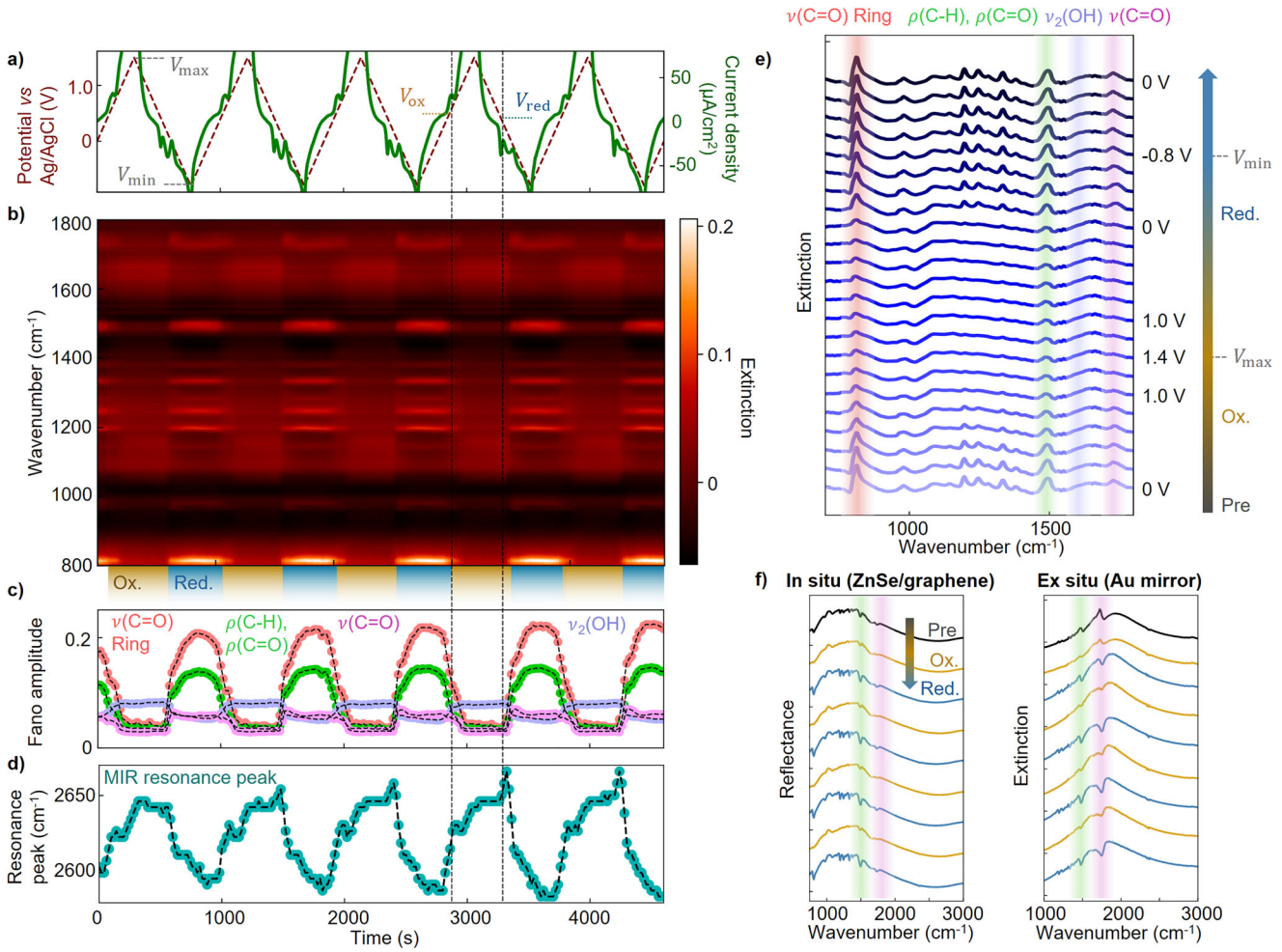



**FIGURE 2** | (a) Cyclic voltammetry over five cycles. (b) SEIRA spectro-electrochemistry showing regeneration of substrate over five cycles of oxidation (yellow shaded, below) and reduction (blue shaded). (c) Fano-fitted CB[5] vibrational resonances (red, green, pink) and water absorption (purple). (d) Change in peak position of MLagg mid-IR resonance during cycling. (e) SEIRA spectra over a single regeneration cycle, vibrational resonances as indicated. (f) Comparison of in situ and ex situ electrochemical regeneration. In (c),(e), $\nu$ represents IR stretching and $\rho$ rocking vibrations, assignments from [17].

We find that all CB[5] vibrational resonance changes correlate with the CV when the MLagg is oxidized (Figure 2c,e), nearly fully disappearing (reduced by >80%). Moreover, rapid recovery of gap-bound species is seen even in these layered closely-packed nanostructures when sweeping the voltage between oxidation and reduction at <10 $mVs^{-1}$ scan rates [28], suggesting that diffusion into the nanogap hotspots is maintained. However, in comparison to electrochemical cleaning of CB[5] from 1–2ML MLaggs as detected in SERS where all signals are removed, these thicker 7–8ML SEIRA structures do not fully remove surface-bound CB[5]. This may be due to the tortuosity and layering of these structures [26]. Indeed, similar results are found with ex situ (oxidized in situ, dried, then analyzed) SEIRA measurements of 7–8ML MLaggs on a gold mirror (Figure 2f), suggesting stacked MLaggs may reclean differently in their different layers. The regeneration performance may hence be further improved by using larger nanoparticles requiring fewer layers and introducing flow to remove desorbed analytes.

A repeatable blue-shift of the MLagg MIR resonance is observed as the sample is oxidized in situ (Figure 2d,f), however, when analyzed ex situ (oxidized in situ, dried, then analyzed), the resonance is seen to red-shift, which suggests an undesirable structural reconfiguration as the sample is dried (Figure 2f and Figures S9 and S10). Moreover, for the latter, a gradual decrease in CB[5] SEIRA strength, changes in Fano lineshape, and broadening of the MIR resonance are seen, indicating progressive sintering [29]. No such effect is visible when cycling in situ, showing this is preferable.

## 2.3 | MIR Resonance Shift Tracks Reconfiguration of Au Surfaces

As the MLagg is oxidized and reduced, its MIR resonance changes in a characteristic and repeatable manner, indicating subtle changes to the nanoparticle surface (Figures 2d and 3a,b). We observe a blue-shift as the sample is oxidized, which is reversed when the MLagg is reduced (Figure S11).

We observe a strong correlation between these shifts in the MIR resonance peak frequency (blue, Figure 3c) and the



16136829, 0, Downloaded from https://onlinelibrary.wiley.com/doi/10.1002/smll.76283 by JEREMY BAUMBERG - Cambridge University Library , Wiley Online Library on [16/10/2026]. See the Terms and Conditions (https://onlinelibrary.wiley.com/terms-and-conditions) on Wiley Online Library for rules of use; OA articles are governed by the applicable Creative Commons License

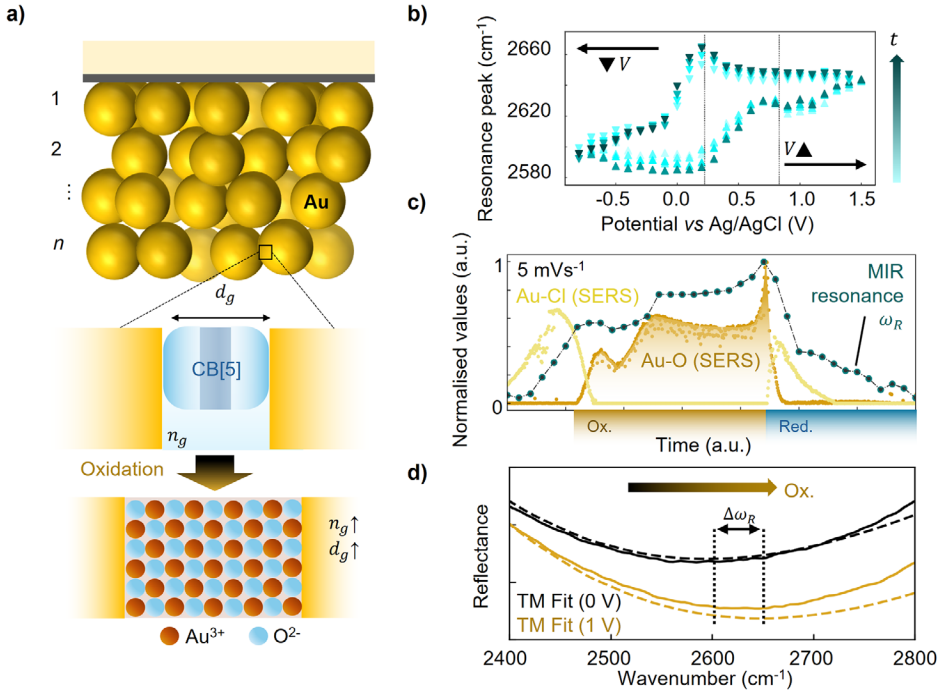



**FIGURE 3** | (a) Shifts in MIR resonance peak position over successive cycles vs. applied potential. (b) Schematic changes in gap size and refractive index as CB[5] is replaced by Au(III) oxide ($Au_2O_3$) during oxidation. (c) Comparison of SERS Au-O and Au-Cl signals (lines, equivalent experimental conditions, 1–2ML MLagg on FTO, corrected for different open circuit potential on FTO and graphene) through an ox/red. cycle, as well as SEIRA resonance peak position (blue points), which is dependent on the gap refractive index and changes with the presence Au-O and Au-Cl. (d) Combined transfer matrix (TM) and dielectric oscillator model (including Au-O), before and after oxidation, showing shift $\Delta\omega_R$ in reflectance dip.

strength of the $Au_2O_3$ peak area in SERS of MLaggs on FTO (brown) [21]. This provides evidence that the MIR spectral shifts track nanoscale changes of the gap contents (as illustrated in Figure 3a). Gold chloride (Au-Cl), which is present in the CB[5] reagent (as previously measured in XPS [28]) and mediates nanoparticle regeneration [28, 30], further influences the resonance position, as its coating of the nanoparticle surface at positive potentials [28] leads to changes in the surrounding dielectric environment, also giving strong SERS signals.

We attribute the increase in resonance frequency during oxidation to a combination of: (i) an increase in the size of the gap between Au(0) surfaces of the nanoparticles (Figure 3a) [19], (ii) an increase in the metamaterial effective refractive index as gold oxide fills the gaps [26], and (iii) the introduction of multiple strong broad infrared-active $Au_2O_3$ absorption lines [28, 31] (DFT simulation Figure S12) resulting from lattice vibrations at ~600 cm$^{-1}$ whose tail affects the MIR resonance position (Figure S13). By fitting a dielectric oscillator model to the gold oxide IR peak (see discussion Note S1), we find that indeed increasing lower-frequency $Au_2O_3$ absorption shifts the MIR resonance to higher frequency (Figure 3d).

We obtain similar effects by fitting the metamaterial effective refractive index and gap thickness to match the final shift in resonance. While an increase in refractive index will red-shift the resonance, an increase in gap size due to the conversion of several gold monolayers to Au(III) oxide leads to a lower effective refractive index, blue-shifting the resonance [26]. Previous estimates show that the gap increases from 0.9 to 1.8 nm due to the formation of two to three atomic layers of Au(III) oxide (previously confirmed by XPS [28]). The change in the effective metamaterial index $n_{\text{eff}}$ due to this change in gap refractive index $n_g$ has been previously [26] modelled with the Maxwell-Garnett effective medium approximation by:

$$n_{\text{eff}}^2 = n_g^2 \frac{1+2f}{1-f} \quad (1)$$

The change in fill fraction $f$ from a gap size of 0.9–1.8 nm in a hexagonal close-packed lattice is from 0.72 to 0.68. Based on this change and the measured ~3% change in resonance frequency, we estimate an increase in the gap refractive index by ~8% based on an initial estimate of $n_{\text{eff}} \approx 3.1$ and $n_g \approx 1.1$ from previous fitting [17, 26] (see discussion Note S1). The sensitivity to tracking changes in the nanogap refractive index based on this model thus amounts to ~1400 nm/RIU, using the effective medium approximation, fitted refractive index and the underlying assumptions for gap size, fill fraction and gap refractive index mentioned above. While this sensitivity is derived from a model and not directly calibrated (since difficult to validate in nanoconfined environments due to different permittivities compared to the bulk), we can put it into context with other detection systems. Fiber-based SPR systems have calibrated refractive index sensitivities >1000 nm/RIU in the visible, multilayer grating based SPR sensors ~300-2500 nm/RIU in the visible [32], and qBIC metasurfaces <500 nm/RIU [33]. Hence, these colloidal metamaterials track sensitively the sub-nanometer changes in surface composition.



16136829, 0, Downloaded from https://onlinelibrary.wiley.com/doi/10.1002/smll.76283 by JEREMY BAUMBERG - Cambridge University Library , Wiley Online Library on [16/10/2026]. See the Terms and Conditions (https://onlinelibrary.wiley.com/terms-and-conditions) on Wiley Online Library for rules of use; OA articles are governed by the applicable Creative Commons License

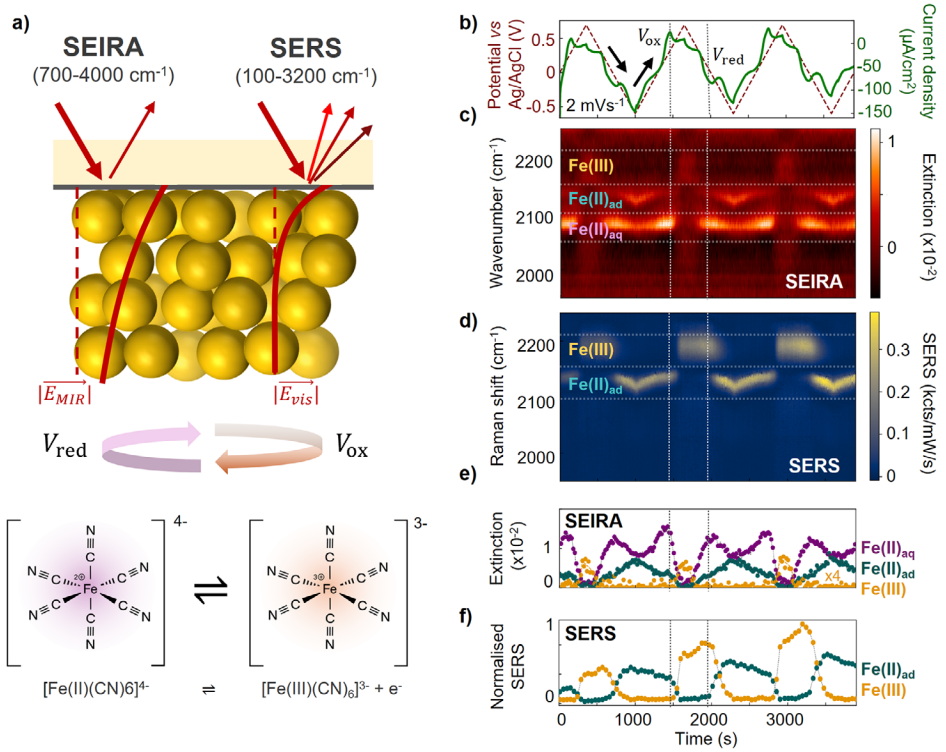



**FIGURE 4** | (a) Schematic of metamaterial modes for SEIRA and SERS, with field distributions at the MIR and visible wavelengths. (b) Cyclic voltammetry of ferro/ferricyanide $[Fe(II)(CN)_6]^{4-}/[Fe(III)(CN)_6]^{3-}$ redox couple (5 mM in 500 mM KPB), over three cycles; dashed lines indicate position of ferricyanide oxidation and reduction peaks. (c,d) Spectro-electrochemistry of ferrocyanide couple with (c) SEIRA extinction and (d) SERS. (e,f) Extracted fits of (e) SEIRA and (f) normalized SERS peak areas.

## 2.4 | Complementary Molecular Sensing With SERS and SEIRA at Nanoscale Interfaces

These EC-devices are versatile sensors to access chemical mechanistic insights involving interfacial reaction dynamics. By using MLaggs as the working electrode, molecules can interact with the gold surface in many ways, including adsorption and electron transfer. Here we use complementary SEIRA and SERS on the same device architecture (in each case using 5 depositions of MLaggs on ZnSe and graphene, measurements taken through the substrate side on two separate samples and separate IR and Raman microscopes) to sense the coordination compound ferrocyanide (Figure 4a), $[Fe(II)(CN)_6]^{4-}$, down to concentrations <5 mM in 500 mM potassium phosphate buffer (KPB) with high signal-to-noise for SEIRA and SERS (Figure S14), though SERS with these MLaggs enables much lower sub-μM LODs [34] and SEIRA sub-mM detection of analytes (Figure S1). We probe electron transfer as it switches its redox state to become ferricyanide, $[Fe(III)(CN)_6]^{3-}$ (Figure 4a). Cycling the redox couple from −0.7 to +0.6 V at 2 $mVs^{-1}$ (Figure 4b) shows both changes in oxidation state and surface interactions whilst keeping the potential below that for gold oxidation. We confirm that the cyclic voltammetry is similar to that on planar FTO, showing that the redox couple behaves in an expected manner on these metamaterial sensors (Figure S15).

Through cyclic voltammetry combined with SEIRA and SERS measurements, we observe subtle changes in the interaction of the various ferricyanide species on the electrode surface. We see strong $[Fe(II)(CN)_6]^{4-}$ signals in both SEIRA and SERS despite the additional presence of CB[5] and counter-cations. Firstly, we observe a $[Fe(II)(CN)_6]^{4-}$ $\nu$(C≡N) mode at ~2065 $cm^{-1}$ that is SEIRA-active but SERS-inactive. The second $[Fe(II)(CN)_6]^{4-}$ $\nu$(C≡N) mode at 2115 $cm^{-1}$ is both SEIRA- and SERS-active. A third $[Fe(III)(CN)_6]^{3-}$ $\nu$(C≡N) mode at ~2170 $cm^{-1}$ is stronger in SERS than SEIRA. We also track the decrease in characteristic CB[5] lines after immersion in $[Fe(II)(CN)_6]^{4-}$ solution, resulting from adsorption of $[Fe(II)(CN)_6]^{4-}$ and desorption of CB[5] (Figure S14). Further data collected in the SERS low-wavenumber spectral region reveal peaks for Fe-C and Fe-C≡N-Au modes (Figure S16).

By comparing these highly sensitive SEIRA measurements to SERS on MLaggs, we obtain detailed complementary information about the redox couple. Key puzzles in this data are (i) a Stark-shifting mode appearing in both SERS and SEIRA at 2115 $cm^{-1}$; (ii) the different potential dependence of the same Fe(III) 2170 $cm^{-1}$ mode in SERS and SEIRA; and (iii) the different potential dependence of different infrared-active Fe(II) modes at 2065 and 2115 $cm^{-1}$.

## 2.5 | Mechanism of Ferrocyanide Couple in Nanogaps

We perform DFT of likely configurations (Figure 5a,b). From the experiment, we find one vibrational mode (2115 $cm^{-1}$) that is common to both SEIRA and SERS. This contrasts with the



16136829, 0, Downloaded from https://onlinelibrary.wiley.com/doi/10.1002/smll.76283 by JEREMY BAUMBERG - Cambridge University Library , Wiley Online Library on [16/10/2026]. See the Terms and Conditions (https://onlinelibrary.wiley.com/terms-and-conditions) on Wiley Online Library for rules of use; OA articles are governed by the applicable Creative Commons License

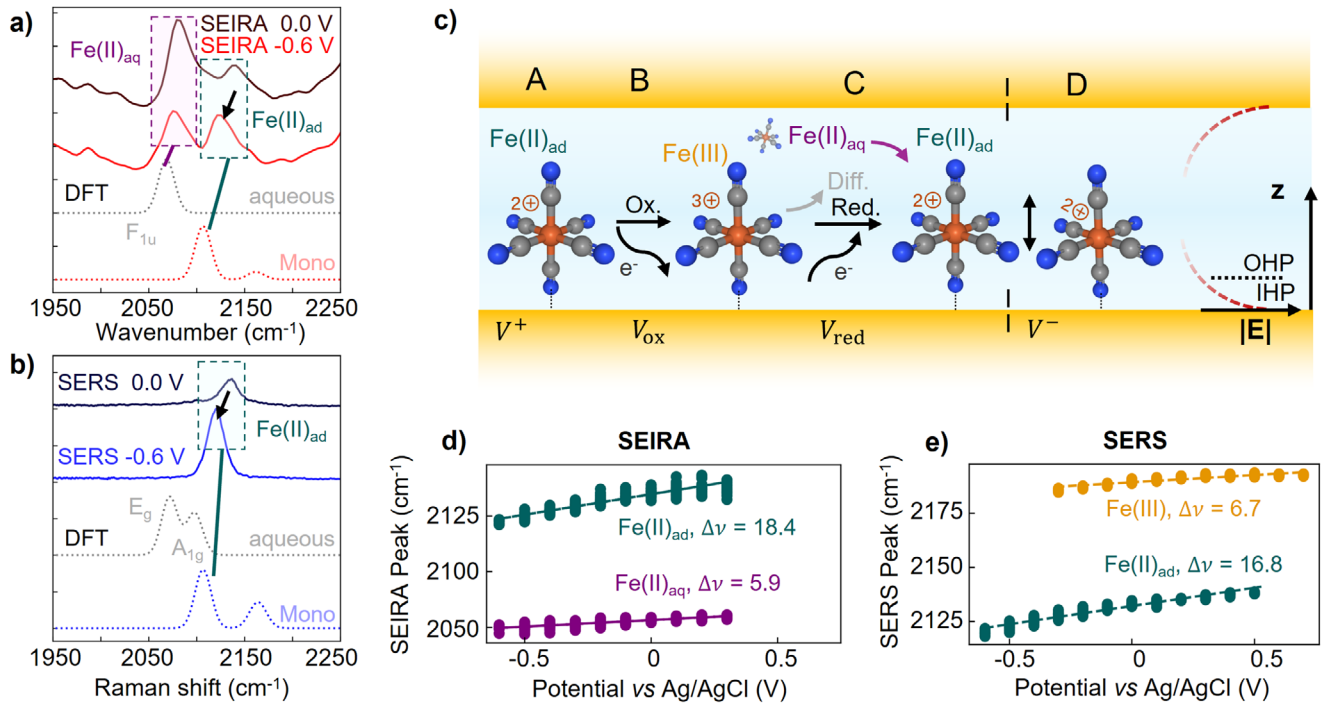



**FIGURE 5** | (a,b) Change in (a) SEIRA and (b) SERS at different potentials, with DFT simulated peaks for solution-phase (aqueous) and polarized DFT aligned along normal to metal surface for Fe(II) adsorbed species, bound by one N (monopod). (c) Schematic of ferro-/ferricyanide species on the charged gold nanoparticle surface, with alphabetic labels to guide the reader; OHP, outer Helmholtz plane; IHP, inner Helmholt plane. (d,e) Extracted peak shifts for (d) SEIRA and (e) SERS.

calculated normal modes for isolated ferrocyanide in the mid-IR ($F_{1u}$) and Raman ($A_{1g}$, $E_g$) with complementary symmetries [35] (Figure 5a,b and Figures S17–S19). This peak is blue-shifted compared to the calculated normal modes, which is indicative of close proximity of the cyanide functional groups to the gold NP surface (Figure 5c, labelled A), resulting in a bridged C≡N-Au mode (that we thus term $Fe(II)_{ad}$) [36]. From polarized DFT (vibrational modes aligned with the field normal to the metal surface are selected), the $\nu$(C≡N) mode indeed shifts to higher wavenumbers due to $\sigma$-donation to the N-Au (Figure 5d,e). Conversely, this leads to a red-shift in the Fe-C low-frequency mode, which we also observe both in our data and DFT (Figures S16 and S17) [37]. Low-wavenumber SERS further reveals the emergence of multiple bands linked to ferrocyanide-metal bridging (Figures S16 and S18).

A likely interpretation for the emergence of a peak that is both IR- and Raman-active lies in the broken symmetry of ferrocyanide close to metallic surfaces. Related observations have been seen in the SERS and SEIRA of CB[5] in MLaggs [17] and for other coordination compounds such as tungsten hexacarbonyl [38]. In a nanogap 0.9 nm wide, ferrocyanide is most likely present as a monolayer between the two AuNP surfaces (as its length is 0.62 nm [35]). At these distances, we expect distortion of the octahedral symmetry of ferricyanide [36], as previously demonstrated in SERS [37] and IR [24] alone using roughened electrodes, which lack the precise faceting of AuNPs. The bridging interaction of the AuNP surface with ferrocyanide leads to different orientational configurations (some explored in Figures S17 and S18). The monopod configuration (one nitrogen atom bound to the gold surface) shows the best agreement between DFT and SEIRA/SERS (Figure 5a–c and Figure S17). We here expect the emergence of one common Raman- and IR-active mode, A1, with additional Raman- and IR-active modes (as shown in the data and polarized DFT, Figure 5d,e). These other possible modes do not appear in SEIRA/SERS due to surface-selection rules (the optical fields are always predominantly normal to the metal) [38].

Comparing the vibrational peak shifts for the different species (Figure 5d,e), we note that the A1 mode of $Fe(II)_{ad}$ exhibits a significant nonlinear shift, whereas the $Fe(II)_{aq}$ seen only in SEIRA does not. The main origin is a change in the binding strength of the Au-N coordination bond, which modulates the peak frequency (as sketched in Figure 5c, labelled D). The counter-ions in the EDL may further screen the cyanide bond adjacent to the gold surface, changing the polarizability of ferrocyanide. We assign the additional lower-wavenumber peak (2065 $cm^{-1}$) in SEIRA to the solution-phase $Fe(II)_{aq}$ species, which has no broken symmetry and thus appears only in SEIRA. Further evidence lies in its smaller Stark shift, which only occurs close to the electrode surface. No SERS-active solution-phase species are observed, likely due to the stronger concentration of the field in the nanogap for SERS compared to SEIRA, which probes further out of the nanogap. The correlated changes in $Fe(II)_{ad}$ and $Fe(II)_{aq}$ across the potential cycle can be understood by considering the diffusion layer within the MLagg. For the MLagg at more negative potentials, more Fe(II) adsorbs at the gold (Figure 5c, labelled C), leading to an increase in the local $Fe(II)_{ad}$ concentration and corresponding decrease in the $Fe(II)_{aq}$ signal (Figure S20). This forms a diffusion layer whose dynamics are hence monitored with SEIRA.



16136829, 0, Downloaded from https://onlinelibrary.wiley.com/doi/10.1002/smll.76283 by JEREMY BAUMBERG - Cambridge University Library , Wiley Online Library on [16/10/2026]. See the Terms and Conditions (https://onlinelibrary.wiley.com/terms-and-conditions) on Wiley Online Library for rules of use; OA articles are governed by the applicable Creative Commons License

As $Fe(II)_{ad}$ is rapidly oxidized, Fe(III) builds up, and Fe(II) is depleted (Figures 4c–e and 5c, labelled B), indicated by the 2170 $cm^{-1}$ mode. Our data suggest that again surface-bound species are present, this time for Fe(III), with symmetry breaking allowing both Raman and IR absorption (Figure S18). Surprisingly, as the applied potential reverses, SERS and SEIRA show the Fe(III) disappearing at different potentials, despite their similar peak positions. This implies that during this reduction to Fe(II), Fe(III) species are located in different regions, with some remaining in the diffusion layer and getting reduced at lower potentials (Figure 4b). We propose that the different potential thresholds seen in SERS and SEIRA stem from the distinct optical field envelopes of SERS and SEIRA (Figure 4a and Figures S4 and S5), with SEIRA probing much further into the MLagg where the potential can be lower than at the graphene contact due to the potential drop between individual gold nanoparticles.

We note that this model and the DFT do not fully replicate the interfacial environment at the electrode. Simulations are generally not capable of capturing the full complexity of analyte-ion-solvent interactions at charged surfaces. Several other possible contributions could thus affect the observed signal. The signal might emerge from other adsorbed species, such as Au-C≡N from cyanide dissociation. These species, however, are found not to be responsible for observed signals based on their characteristic low-frequency signatures, linear Stark shifts, and distinct potential-dependence [8, 39–43], as well as clear redox transitions and Fe-C peaks from the ferrocyanide molecule. The signal is further unlikely to be caused by crystallised ferrocyanide whose formation is irreversible [24] (unlike the signal attributed to $Fe(II)_{ad}$), or crystallization intermediates found at lower wavenumbers and showing a different potential dependence [18]. The Stark effect observed in SEIRA and SERS could have other causes, for instance molecular reorganization or various interactions with the EDL. The structure of the EDL in nanoconfined environments is highly complex [44], changes due to ion-analyte interactions, and affects the electric field experienced by the analyte [34].

Despite the well-studied nature of this ferrocyanide redox couple, we show here that combining surface-enhanced IR and Raman spectroscopies reveals more than previously known about symmetry breaking of molecules at electrode surfaces. Detailed spectro-electrochemistry results give new data to test against a variety of theoretical models, that moreover, should combine both surface binding, ionic details of the EDL, as well as dynamics of the diffusion layer. It shows how the complementarity of SEIRA and SERS can be exploited in a multiplexed platform for future studies of different molecules, such as in novel battery electrolytes.

## 3 | Conclusion

This study presents an architecture to perform real-time combined SEIRA and SERS measurements on a plasmonically-active metamaterials device. It presents the first electrochemical regeneration method for SEIRA substrates, evidenced by the replacement of the molecular linker molecule by an atomically thin layer of gold oxide, whose generation can be monitored through changes in the nanogap effective refractive index. These results further demonstrate the potential of using complementary electrochemistry, SEIRA, and SERS measurements on the same flow device, allowing for easier and more reliable measurement and analysis of redox reactions. We emphasize that tracking such symmetry-breaking behavior on metallic electrode surfaces is of great interest in plasmonic catalysis and plasmon-driven chemistry, as well as real-time monitoring of the pharmaceutical production of bioproducts [45, 46].

## 4 | Methods

### 4.1 | Graphene Substrate Fabrication

The ZnSe substrate was oxygen plasma cleaned for 5 s (oxygen mass flow of 30 sccm, 90% RF power) using a plasma etcher (Diener electronic GmbH & Co. KG) to remove surface-bound organics and improve its hydrophilicity. The monolayer Trivial Transfer CVD graphene (ACS Materials) was then transferred onto the clean ZnSe substrate, dried for 2 h and then baked for 20 min at 100°C. Subsequently, the PMMA adhesion layer was dissolved by immersion in acetone for 24 h, rinsed, 15 min, rinsed, 5 min, rinsed. Graphene quality and the removal of PMMA residues were checked with Raman spectroscopy, using a Renishaw InViva Raman confocal microscope, using a 100x objective and 1200 lines $mm^{-1}$ grating, and a 532 nm excitation laser. A gold contact was thermally evaporated (2 nm Cr, 50 nm Au) using a shadow mask with a deposition rate <0.5 Å/s. The contact was then attached to a Pt wire via Field's metal heated to 65°C, forming a stable connection. Finally, the contact was insulated with nail varnish, leaving only the pristine graphene exposed.

### 4.2 | Multilayer Aggregate Formation

100 and 250 nm gold (BBI Solutions) nanoparticles were mixed in an Eppendorf tube to make up a total of 500 µL of nanoparticles. 500 µL of chloroform ($CHCl_3$) was then added to another Eppendorf, followed by 500 µL of the nanoparticle mixture. 100 µL of 1 mM cucurbit[5]uril (CB[5]) solution was then added and shaken for ∼1 min to initiate aggregation. The mixture was left to settle for the immiscible $CHCl_3$ and aqueous phases to separate and the aggregated AuNPs to move to the phase interfaces (chloroform-aqueous and aqueous-air). The aqueous phase was washed with three 300 µL aliquots of DI water to dilute the citrate salts and other supernatants, then concentrated by careful removal of the aqueous phase to form a ∼5 µL aggregate droplet floating on the $CHCl_3$. The droplet was deposited onto the graphene substrate and left to dry. Once dried, the resulting AuNP multilayer aggregate was rinsed with DI water and dried with $N_2$. This was repeated another 4 times, depositing the new aggregate droplet in the same position each time for a total of 5 depositions to give a sample with multiple layers of nanoparticles.

### 4.3 | Electrochemical Measurements

The sample was immersed in an electrochemical flow cell. The cell is fabricated out of 10:1 PDMS:cross-linker, and its



16136829, 0, Downloaded from https://onlinelibrary.wiley.com/doi/10.1002/smll.76283 by JEREMY BAUMBERG - Cambridge University Library , Wiley Online Library on [16/10/2026]. See the Terms and Conditions (https://onlinelibrary.wiley.com/terms-and-conditions) on Wiley Online Library for rules of use; OA articles are governed by the applicable Creative Commons License

geometry adjusted via biopsy punches to include a well with a diameter of 6 mm, inlet and outlet, as well as inserts for electrodes. The three-electrode amperometric system included a Pt counter electrode and Ag/AgCl reference electrode. The sample was used as the working electrode. The current density was obtained by dividing the current by the area of the exposed working electrode (~0.28 $cm^2$). Measurements were performed using a portable potentiostat (CompactStat) from Ivium Technologies.

### 4.4 | Plasma Cleaning

The MLaggs are oxygen plasma cleaned for 45 min (oxygen mass flow of 30 sccm, 90% RF power) using a plasma etcher (Diener electronic GmbH & Co. KG) to remove CB[5], citrate and other supernatants from the AuNP surfaces (verified using SERS). To re-introduce a scaffolding ligand, the MLaggs are immersed in equal volumes of 1 mM CB[5] or CB[7] solution and 1 M HCl for 5 min. In both cases, the MLaggs are rinsed with DI water and dried with $N_2$.

### 4.5 | Infrared Microscopy

All samples are analyzed in a Shimadzu AIM-9000 infrared microscope, linked to a Shimadzu IR-Tracer 100. For image acquisition, a spectral resolution of 8 $cm^{-1}$, and aperture size of 200 × 200 $\mu m^2$ and a sample number of 16–32 are used. Spectra of the aggregates are registered to the same spot in the bright-field. Post-processing involves filtering with a linear, third-order Savitzky-Golay filter, restricting the wavenumber range of the spectrum, and background-subtraction by fitting with a second-order polynomial. The peak position of the MIR resonance is extracted by fitting a Voigt function to the spectrum. The amplitude, peak position and phase of the Fano resonances are extracted using a physical fit (Figure S21).

### 4.6 | Raman Microscopy

SERS measurements were collected on a Renishaw InViva Raman confocal microscope, using a 20× objective (NA = 0.4) and 1200 lines $mm^{-1}$ grating. To collect the lower wavenumber spectral regions, the 785 nm excitation laser was used in extended scan mode, with 1 s integration time and 0.5% laser power (2.2 mW at the sample). All measurements were taken at room temperature, and the spectra were calibrated with respect to Si. Spectra were analyzed using Python, and any background removed by iteratively fitting a polynomial to the base of the peaks.

### 4.7 | Characterization

Scanning electron microscope (SEM) imaging of MLaggs deposited on graphene and ZnSe uses a FEI Philips Dualbeam Quanta 3D SEM (dwell 3–10 μs, HV 2 kV, current 50 pA, and ≈3.0 mm working distance).

### 4.8 | Density Functional Theory (DFT) Calculations

DFT calculations on ferrocyanide were performed using the B3LYP [47, 48] hybrid generalized gradient approximation exchange-correlation functional, augmented with Grimme's D3 dispersion correction and Becke-Johnson damping (GD3BJ) [49]. The def2-TZVP basis set was employed for all atoms [50].

For surface-bound species, Au atoms were explicitly placed at the terminal N atoms of coordinated cyanide ligands to model monopod, bipod, and linear adsorption configurations. No implicit solvation model or structural constraints were applied, and all atomic coordinates were fully relaxed during geometry optimization. The charge, multiplicity, and number of Au atoms for each model are summarized in Table S1.

A DFT scaling factor of 0.985 was applied to all calculated vibrational frequencies, and the peaks broadened with a Gaussian fit. All DFT calculations were implemented using an ultrafine integration grid in Gaussian 09 Rev. E [51]. Due to the local plasmonic near field orientation being vertical to the gold surface, the IR and Raman modes for the adsorbed species will have different intensities relative to an isotropic system. These were calculated using the methodology in [52] from the IR dipoles and Raman tensors extracted from the DFT simulations.

DFT calculations on $Au_2O_3$ were carried out using the Vienna Ab initio Simulation Package (VASP) [53–55] with core-valence electron interactions described via the projector augmented wave (PAW) method [56]. The Au and O pseudopotentials were taken from the PAW_PBE_64 library. All calculations employed the PBEsol exchange-correlation functional [57] with a Hubbard U parameter of 0.702 eV applied to the Au d orbitals [58] to account for localized electron correlation. A plane wave cutoff energy of 600 eV was used (increased to 780 eV for variable-cell calculations), with a k-point sampling density of 0.32 $Å^{-1}$. Atomic positions were optimized until residual forces fell below $5 \times 10^{-4}$ eV $Å^{-1}$. Force constants and IR intensities were computed using phonopy [59, 60] and the phonopy-spectroscopy package [61] for pre- and post-processing of the lattice dynamics calculations.

### 4.9 | COMSOL Simulations

To calculate the field enhancement and the effective refractive index of the metamaterial, we conduct frequency domain simulations. The simulation domain is a hexagonal unit cell, with Floquet periodic boundary conditions applied on the sides and a perfectly matched layer applied at the top and bottom. An incoming port is added at the bottom to launch the excitation and obtain the complex reflection coefficient, and an outgoing port is added at the top to obtain the complex transmission coefficient. The ports are set to be half a wavelength away from the metamaterial layer. The metamaterial layer is set in air, and it consists of the plasmonic gold resonator with diameter $D$, embedded in a slab of refractive index $n = 1.5$, thickness $d$. The effective refractive index of the metamaterial is found



16136829, 0, Downloaded from https://onlinelibrary.wiley.com/doi/10.1002/smll.76283 by JEREMY BAUMBERG - Cambridge University Library , Wiley Online Library on [16/10/2026]. See the Terms and Conditions (https://onlinelibrary.wiley.com/terms-and-conditions) on Wiley Online Library for rules of use; OA articles are governed by the applicable Creative Commons License

from the complex reflection and transmission coefficients by a standard inversion technique [62]. The field enhancement is extracted along the center line of a boundary of the unit cell. To calculate the decay of the field inside the homogeneous slab we set its thickness to $d = 677$ nm (corresponding to 8 layers of tightly packed nanoparticles) and, based on the retrieved effective parameters at $\lambda = 785$ nm we set its refractive index to $n = 4.7 + 3.7i$.

### Author Contributions

N.S., T.J., S.M.S.T, R.A. and J.J.B conceived and designed the experiment. N.S., T.J. and S.M.S.T. performed the fabrication and spectroscopic experiments with input from R.A. and Y.R., with C.T. and S.Z. aiding the characterization. N.S. and T.J. analyzed the data with input from J.J.B., R.A., I.Q.L. Simulations and analytical modelling were carried out by Z.S., A.S., N.S., T.J. and C.T. All authors contributed to writing and editing the manuscript.


### Acknowledgements

The authors acknowledge financial support from the European Research Council (ERC) under Horizon 2020 research and innovation programme PICOFORCE (Grant Agreement No. 883703), from the UKRI (UKRI3173, UKRI129885R) and from the EPSRC (Cambridge NanoDTC EP/L015978/1, EP/X037770/1, EP/Y008162/1, EP/Y036379/1, UKRI1255). N.S. acknowledges support from EPSRC Grant EP/L015889/1 for the EPSRC Centre for Doctoral Training in Sensor Technologies and Applications, and from AstraZeneca (MedImmune Ltd). S.M.S.-T. is supported by the Harding Distinguished Scholarship Programme and Magdalene College, Cambridge. C.T. is supported by a Gates Cambridge fellowship (OPP1144). R.A. acknowledges support from the Winton Programme for the Physics of Sustainability and from St. John's College, Cambridge. A.D. wishes to acknowledge support from the Royal Society University Research Fellowship URF/R1/180097 and URF/R/231024, Royal Society Research Fellows Enhancement Award RGF /EA/181038, funding from EPSRC grants EP/Y008774/1 and EP/X012689/1, and for the CDT in Topological Design EP/S02297X/1. Q.L. acknowledges support from the Dutch Research Council (NWO OCENW.XS24.2.142, 24.4.328) and PhotonDelta (NGF.1708.25.029). The $Au_2O_3$ DFT computations done in this work were performed using the University of Birmingham's BlueBEAR HPC service, the Baskerville Tier 2 HPC service (https://www.baskerville.ac.uk/; funded by the EPSRC and UKRI through the World Class Labs scheme (EP/T022221/1) and the Digital Research Infrastructure programme (EP/W032244/1)), and the Sulis Tier 2 HPC platform hosted by the Scientific Computing Research Technology Platform at the University of Warwick (funded by EPSRC Grant EP/T022108/1 and the HPC Midlands+ consortium). Through our membership of the UK EPSRC HEC Materials Chemistry Consortium (EPSRC; EP/L000202, EP/R029431, EP/T022213), this work also used ARCHER2 UK National Supercomputing Services. We are also grateful to the UK Materials and Molecular Modelling Hub for computational resources, which is partially funded by EPSRC (EP/T022213/1, EP/W032260/1 and EP/P020194/1).


### Conflicts of Interest

The authors J.J.B., S.M.S.-T. and R.A. declare the following competing interests: filed patents, Surface-enhanced spectroscopy substrates, UK 2304765.7, 30/3/2023; Detection method and in-flow Detection Method, UK Patent Application No: 2418909.4, 20/12/2024.

### Data Availability Statement

The data that support the findings of this study are available in the supplementary material of this article and on the Cambridge Open Data archive.

### References


1. D. Lyu, J. Xu, and Z. Wang, "Time-Resolved in Situ Vibrational Spectroscopy for Electrocatalysis: Challenge and Opportunity," *Frontiers in Chemistry* 11 (2023): 1231886, https://doi.org/10.3389/fchem.2023.1231886.

2. F. Le, D. W. Brandl, Y. A. Urzhumov, et al., "Metallic Nanoparticle Arrays: A Common Substrate for both Surface-Enhanced Raman Scattering and Surface-Enhanced Infrared Absorption," *ACS Nano* 2, no. 4: 707–718, https://doi.org/10.1021/nn800047e.

3. E. Oksenberg, I. Shlesinger, G. Tek, A. F. Koenderink, and E. C. Garnett, "Complementary Surface-Enhanced Raman Scattering (SERS) and IR Absorption Spectroscopy (SEIRAS) With Nanorods-on-a-Mirror," *Advanced Functional Materials* 33, no. 8 (2023): 2211154, https://doi.org/10.1002/adfm.202211154.

4. A. B. Sánchez-Alvarado, J. Zhou, P. Jin, et al., "Combined Surface-Enhanced Raman and Infrared Absorption Spectroscopies for Streamlined Chemical Detection of Polycyclic Aromatic Hydrocarbon-Derived Compounds," *ACS Nano* 17, no. 24 (2023): 25697–25706, https://doi.org/10.1021/acsnano.3c10746.

5. M. Papasizza and A. Cuesta, "In Situ Monitoring Using ATR-SEIRAS of the Electrocatalytic Reduction of $CO_2$ on Au in an Ionic Liquid/Water Mixture," *ACS Catalysis* 8, no. 7 (2018): 6345–6352, https://doi.org/10.1021/acscatal.8b00977.

6. Y. Katayama, F. Nattino, L. Giordano, et al., "An *in* Situ Surface-Enhanced Infrared Absorption Spectroscopy Study of Electrochemical $CO_2$ Reduction: Selectivity Dependence on Surface C-Bound and O-Bound Reaction Intermediates," *The Journal of Physical Chemistry C* 123, no. 10 (2019): 5951–5963, https://doi.org/10.1021/acs.jpcc.8b09598.

7. S. Zhu, B. Jiang, W.-B. Cai, and M. Shao, "Direct Observation on Reaction Intermediates and the Role of Bicarbonate Anions in $CO_2$ Electrochemical Reduction Reaction on Cu Surfaces," *Journal of the American Chemical Society* 139, no. 44 (2017): 15664–15667, https://doi.org/10.1021/jacs.7b10462.

8. X. Chang, S. Vijay, Y. Zhao, N. J. Oliveira, K. Chan, and B. Xu, "Understanding the Complementarities of Surface-Enhanced Infrared and Raman Spectroscopies in CO Adsorption and Electrochemical Reduction," *Nature Communications* 13 (2022): 2656, https://doi.org/10.1038/s41467-022-30262-2.

9. L. M. Berger, M. Duportal, L. D. S. Menezes, et al., "Improved In Situ Characterization of Electrochemical Interfaces Using Metasurface-Driven Surface-Enhanced IR Absorption Spectroscopy," *Advanced Functional Materials* 33, no. 25 (2023): 2300411, https://doi.org/10.1002/adfm.202300411.

10. M. Duportal, L. M. Berger, S. A. Maier, A. Tittl, and K. Krischer, "Multi-Band Metasurface-Driven Surface-Enhanced Infrared Absorption Spectroscopy for Improved Characterization of in-Situ Electrochemical Reactions," *ACS Photonics* 11, no. 2 (2024): 714–722, https://doi.org/10.1021/acsphotonics.3c01592.

11. J. P. Vivek, N. G. Berry, J. Zou, R. J. Nichols, and L. J. Hardwick, "In Situ Surface-Enhanced Infrared Spectroscopy to Identify Oxygen Reduction Products in Nonaqueous Metal–Oxygen Batteries," *The Journal of Physical Chemistry C* 121, no. 36 (2017): 19657–19667, https://doi.org/10.1021/acs.jpcc.7b06391.

12. M. Shao, P. Liu, and R. R. Adzic, "Superoxide Anion Is the Intermediate in the Oxygen Reduction Reaction on Platinum Electrodes," *Journal of the American Chemical Society* 128, no. 23 (2006): 7408–7409, https://doi.org/10.1021/ja061246s.

13. O. J. R. Clarke, A. Rowley, R. V. Fox, A. Atifi, and I. J. Burgess, "Diamonds in the Rough: Direct Surface Enhanced Infrared Spectroscopic Evidence of Nitrogen Reduction on Boron-Doped Diamond Supported Metal Catalysts," *Analytical Chemistry* 95, no. 28 (2023): 10476–10480, https://doi.org/10.1021/acs.analchem.3c01638.

14. H. Zhang, B. Chen, T. Liu, G. W. Brudvig, D. Wang, and M. M. Waegele, "Infrared Spectroscopic Observation of Oxo- and Superoxo-Intermediates in the Water Oxidation Cycle of a Molecular Ir Catalyst," *Journal of the*





16136829, 0, Downloaded from https://onlinelibrary.wiley.com/doi/10.1002/smll.76283 by JEREMY BAUMBERG - Cambridge University Library , Wiley Online Library on [16/10/2026]. See the Terms and Conditions (https://onlinelibrary.wiley.com/terms-and-conditions) on Wiley Online Library for rules of use; OA articles are governed by the applicable Creative Commons License

*American Chemical Society* 146, no. 1 (2024): 878–883, https://doi.org/10.1021/jacs.3c11206.

15. D. Wright, S. Sangtarash, N. S. Mueller, Q. Lin, H. Sadeghi, and J. J. Baumberg, "Vibrational Stark Effects: Ionic Influence on Local Fields," *The Journal of Physical Chemistry Letters* 13, no. 22 (2022): 4905–4911, https://doi.org/10.1021/acs.jpclett.2c01048.

16. D. Bhattacharyya, P. E. Videla, M. Cattaneo, V. S. Batista, T. Lian, and C. P. Kubiak, "Vibrational Stark Shift Spectroscopy of Catalysts Under the Influence of Electric Fields at Electrode–Solution Interfaces," *Chemical Science* 12, no. 30 (2021): 10131–10149, https://doi.org/10.1039/D1SC01876K.

17. R. Arul, D.-B. Grys, R. Chikkaraddy, et al., "Giant Mid-IR Resonant Coupling to Molecular Vibrations in Sub-Nm Gaps of Plasmonic Multilayer Metafilms," *Light: Science & Applications* 11, no. 1 (2022): 281, https://doi.org/10.1038/s41377-022-00943-0.

18. J. Li, D. Wu, J. Li, et al., "Ultrasensitive Plasmon-Enhanced Infrared Spectroelectrochemistry," *Angewandte Chemie International Edition* 63, no. 11 (2024): 202319246, https://doi.org/10.1002/anie.202319246.

19. D.-B. Grys, M. Niihori, R. Arul, et al., "Controlling Atomic-Scale Restructuring and Cleaning of Gold Nanogap Multilayers for Surface-Enhanced Raman Scattering Sensing," *ACS Sensors* 8, no. 7 (2023): 2879–2888, https://doi.org/10.1021/acssensors.3c00967.

20. W. J. Chang, B. J. Roman, A. M. Green, T. M. Truskett, and D. J. Milliron, "Surface-Enhanced Infrared Absorption Spectroscopy by Resonant Vibrational Coupling With Plasmonic Metal Oxide Nanocrystals," *ACS Nano* 18, no. 31 (2024): 20636–20647, https://doi.org/10.1021/acsnano.4c06145.

21. S. M. Sibug-Torres, D.-B. Grys, G. Kang, et al., "In Situ Electrochemical Regeneration of Nanogap Hotspots for Continuously Reusable Ultrathin SERS Sensors," *Nature Communications* 15, no. 1 (2024): 2022.

22. X. Miao, T. S. Luk, and P. Q. Liu, "Liquid-Metal-Based Nanophotonic Structures for High-Performance SEIRA Sensing," *Advanced Materials* 34, no. 10 (2022): 2107950, https://doi.org/10.1002/adma.202107950.

23. M. Baillieul, E. Rinnert, J. Lemaitre, et al., "Surface Functionalization With Polymer Membrane or SEIRA Interface to Improve the Sensitivity of Chalcogenide-Based Infrared Sensors Dedicated to the Detection of Organic Molecules," *ACS Omega* 7, no. 51 (2022): 47840–47850, https://doi.org/10.1021/acsomega.2c05502.

24. C. M. Pharr and P. R. Griffiths, "Infrared Spectroelectrochemical Analysis of Adsorbed Hexacyanoferrate Species Formed During Potential Cycling in the Ferrocyanide/Ferricyanide Redox Couple," *Analytical Chemistry* 69, no. 22 (1997): 4673–4679, https://doi.org/10.1021/ac961120l.

25. Y. Qi, V. Brasiliense, T. W. Ueltschi, et al., "Plasmon-Driven Chemistry in Ferri-/Ferrocyanide Gold Nanoparticle Oligomers: A SERS Study," *Journal of the American Chemical Society* 142, no. 30 (2020): 13120–13129, https://doi.org/10.1021/jacs.0c05031.

26. N. Spiesshofer, E. Wyatt, Z. Sztranyovszky, et al., "Tailoring Ultrahigh Index Plasmonic Combinatorial Metamaterials for SEIRA and SERS by Tuning the Fill Fraction," *Optica* 12, no. 9 (2025): 1357, https://doi.org/10.1364/OPTICA.567324.

27. A. Ambrosi, C. K. Chua, A. Bonanni, and M. Pumera, "Electrochemistry of Graphene and Related Materials," *Chemical Reviews* 114, no. 14 (2014): 7150–7188, https://doi.org/10.1021/cr500023c.

28. S. M. Sibug-Torres, M. Niihori, E. Wyatt, et al., "Transient Au–Cl Adlayers Modulate the Surface Chemistry of Gold Nanoparticles During Redox Reactions," *Nature Chemistry* 18, no. 2 (2026): 294–301, https://doi.org/10.1038/s41557-025-01989-4.

29. M. F. Limonov, M. V. Rybin, A. N. Poddubny, and Y. S. Kivshar, "Fano Resonances in Photonics," *Nature Photonics* 11, no. 9 (2017): 543–554, https://doi.org/10.1038/nphoton.2017.142.

30. S. M. Sibug-Torres, G. Q. Wallace, T. Jones, D. Graham, and J. J. Baumberg, "The role of Au–Cl Adlayers in the Turkevich Synthesis of Gold Nanoparticles," *Chemical Communications* 62 (2026): 5890–5894, https://doi.org/10.1039/D6CC00457A.

31. H. Shi, R. Asahi, and C. Stampfl, "Properties of the Gold Oxides $Au_2O_3$ and $Au_2O$: First-Principles Investigation," *Physical Review B* 75, no. 20 (2007): 205125, https://doi.org/10.1103/PhysRevB.75.205125.

32. R. A. Mahmud, R. H. Sagor, and M. Z. M. Khan, "Surface Plasmon Refractive Index Biosensors: A Review of Optical Fiber, Multilayer 2D Material and Gratings, and MIM Configurations," *Optics & Laser Technology* 159 (2023): 108939, https://doi.org/10.1016/j.optlastec.2022.108939.

33. X. Yang, A. Antonov, H. Hu, and A. Tittl, "Permittivity-Asymmetric qBIC Metasurfaces for Refractive Index Sensing," *Nanophotonics* 14, no. 27 (2025): 5311–5321, https://doi.org/10.1515/nanoph-2025-0415.

34. T. Jones, M. M. Kim, S. M. Sibug-Torres, et al., "How the Electrochemical Double Layer Manipulates Molecule–Metal Interactions," *ACS Nano* 20, no. 25 (2026): 18284–18292, https://doi.org/10.1021/acsnano.6c03605.

35. C. Korzeniewski, M. W. Severson, P. P. Schmidt, S. Pons, and M. Fleischmann, "Theoretical Analysis of the Vibrational Spectra of Ferricyanide and Ferrocyanide Adsorbed on Metal Electrodes," *The Journal of Physical Chemistry* 91, no. 22 (1987): 5568–5573, https://doi.org/10.1021/j100306a015.

36. K. Nakamoto, "*Infrared and Raman Spectra of Inorganic and Coordination Compounds, Part B: Applications in Coordination, Organometallic, and Bioinorganic Chemistry*," (John Wiley & Sons, 2006).

37. R. B. Lowry, "SERS and Fourier Transform SERS Studies of the Hexacyanoferrate(III)-Hexacyanoferrate(II) Couple on Gold Electrode Surfaces," *Journal of Raman Spectroscopy* 22, no. 12 (1991): 805–809, https://doi.org/10.1002/jrs.1250221213.

38. I. Morichika, K. Murata, A. Sakurai, K. Ishii, and S. Ashihara, "Molecular Ground-State Dissociation in the Condensed Phase Employing Plasmonic Field Enhancement of Chirped Mid-Infrared Pulses," *Nature Communications* 10, no. 1 (2019): 3893, https://doi.org/10.1038/s41467-019-11902-6.

39. A. Ge, P. E. Videla, G. L. Lee, et al., "Interfacial Structure and Electric Field Probed by *In Situ* Electrochemical Vibrational Stark Effect Spectroscopy and Computational Modeling," *The Journal of Physical Chemistry C* 121, no. 34 (2017): 18674–18682, https://doi.org/10.1021/acs.jpcc.7b05563.

40. D. Bhattacharyya, P. E. Videla, J. M. Palasz, et al., "Sub-Nanometer Mapping of the Interfacial Electric Field Profile Using a Vibrational Stark Shift Ruler," *Journal of the American Chemical Society* 144, no. 31 (2022): 14330–14338, https://doi.org/10.1021/jacs.2c05563.

41. G. L. Beltramo, T. E. Shubina, S. J. Mitchell, and M. T. M. Koper, "Cyanide Adsorption on Gold Electrodes: A Combined Surface Enhanced Raman Spectroscopy and Density Functional Theory Study," *Journal of Electroanalytical Chemistry* 563, no. 1 (2004): 111–120, https://doi.org/10.1016/j.jelechem.2003.07.040.

42. S. Vijay, T. V. Hogg, J. Ehlers, et al., "Interaction of CO With Gold in an Electrochemical Environment," *The Journal of Physical Chemistry C* 125, no. 32 (2021): 17684–17689, https://doi.org/10.1021/acs.jpcc.1c04013.

43. D. Wright, Q. Lin, D. Berta, et al., "Mechanistic Study of an Immobilized Molecular Electrocatalyst by in Situ Gap-Plasmon-Assisted Spectro-Electrochemistry," *Nature Catalysis* 4, no. 2 (2021): 157–163, https://doi.org/10.1038/s41929-020-00566-x.

44. M. M. Kim, D. H. Kim, J. Cho, S.-J. Shin, C. H. Choi, and H. Kim, "Electric Double Layer Structure in Concentrated Aqueous Solution," *Nature Communications* 17, no. 1 (2026): 3645, https://doi.org/10.1038/s41467-026-70322-5.

45. M. L. Brongersma, R. A. Pala, H. Altug, et al., "The Second Optical Metasurface Revolution: Moving From Science to Technology," *Nature Reviews Electrical Engineering* 2, no. 2 (2025): 125–143, https://doi.org/10.1038/s44287-024-00136-4.



16136829, 0, Downloaded from https://onlinelibrary.wiley.com/doi/10.1002/smll.76283 by JEREMY BAUMBERG - Cambridge University Library , Wiley Online Library on [16/10/2026]. See the Terms and Conditions (https://onlinelibrary.wiley.com/terms-and-conditions) on Wiley Online Library for rules of use; OA articles are governed by the applicable Creative Commons License

46. A. J. El-Helou, Y. Liu, and C. Chen, "Optical Metasurfaces for the Next-Generation Biosensing and Bioimaging," *Laser & Photonics Reviews* 19 (2025): 2401715, https://doi.org/10.1002/lpor.202401715.

47. A. D. Becke, "Density-Functional Thermochemistry. III. The Role of Exact Exchange," *The Journal of Chemical Physics* 98, no. 7 (1993): 5648–5652, https://doi.org/10.1063/1.464913.

48. C. Lee, W. Yang, and R. G. Parr, "Development of the Colle-Salvetti Correlation-Energy Formula Into a Functional of the Electron Density," *Physical Review B* 37, no. 2 (1988): 785–789, https://doi.org/10.1103/PhysRevB.37.785.

49. S. Grimme, S. Ehrlich, and L. Goerigk, "Effect of the Damping Function in Dispersion Corrected Density Functional Theory," *Journal of Computational Chemistry* 32, no. 7 (2011): 1456–1465, https://doi.org/10.1002/jcc.21759.

50. F. Weigend and R. Ahlrichs, "Balanced Basis Sets of Split Valence, Triple Zeta Valence and Quadruple Zeta Valence Quality for H to Rn: Design and Assessment of Accuracy," *Physical Chemistry Chemical Physics* 7, no. 18 (2005): 3297, https://doi.org/10.1039/b508541a.

51. M. J. Frisch, G. W. Trucks, and H. B. Schlegel, *Gaussian 16 Rev. C.01* (Gaussian, 2016).

52. D.-B. Grys, B. De Nijs, A. R. Salmon, et al., "Citrate Coordination and Bridging of Gold Nanoparticles: The Role of Gold Adatoms in AuNP Aging," *ACS Nano* 14, no. 7 (2020): 8689–8696.

53. G. Kresse and J. Hafner, "*Ab Initio* Molecular Dynamics for Liquid Metals," *Physical Review B* 47, no. 1 (1993): 558–561, https://doi.org/10.1103/PhysRevB.47.558.

54. G. Kresse and J. Furthmüller, "Efficiency of Ab-Initio Total Energy Calculations for Metals and Semiconductors Using a Plane-Wave Basis Set," *Computational Materials Science* 6, no. 1 (1996): 15–50, https://doi.org/10.1016/0927-0256(96)00008-0.

55. G. Kresse and J. Furthmüller, "Efficient Iterative Schemes for *Ab Initio* Total-Energy Calculations Using a Plane-Wave Basis Set," *Physical Review B* 54, no. 16 (1996): 11169–11186, https://doi.org/10.1103/PhysRevB.54.11169.

56. G. Kresse and D. Joubert, "From Ultrasoft Pseudopotentials to the Projector Augmented-Wave Method," *Physical Review B* 59, no. 3 (1999): 1758–1775, https://doi.org/10.1103/PhysRevB.59.1758.

57. J. P. Perdew, A. Ruzsinszky, G. I. Csonka, et al., "Restoring the Density-Gradient Expansion for Exchange in Solids and Surfaces," *Physical Review Letters* 100, no. 13 (2008): 136406, https://doi.org/10.1103/PhysRevLett.100.136406.

58. G. C. Moore, M. K. Horton, E. Linscott, et al., "High-Throughput Determination of Hubbard U and Hund J Values for Transition Metal Oxides via the Linear Response Formalism," *Physical Review Materials* 8, no. 1 (2024): 014409, https://doi.org/10.1103/PhysRevMaterials.8.014409.

59. A. Togo, "First-Principles Phonon Calculations With Phonopy and Phono3py," *Journal of the Physical Society of Japan* 92, no. 1 (2023): 012001, https://doi.org/10.7566/JPSJ.92.012001.

60. A. Togo, L. Chaput, T. Tadano, and I. Tanaka, "Implementation Strategies in Phonopy and Phono3py," *Journal of Physics: Condensed Matter* 35, no. 35 (2023): 353001.

61. J. M. Skelton, L. A. Burton, A. J. Jackson, F. Oba, S. C. Parker, and A. Walsh, "Lattice Dynamics of the Tin Sulphides $SnS_2$ , SnS and $Sn_2S_3$: Vibrational Spectra and Thermal Transport," *Physical Chemistry Chemical Physics* 19, no. 19 (2017): 12452–12465, https://doi.org/10.1039/C7CP01680H.

62. X. Chen, T. M. Grzegorczyk, B.-I. Wu, J. Pacheco, and J. A. Kong, "Robust Method to Retrieve the Constitutive Effective Parameters of Metamaterials," *Physical Review E* 70, no. 1 (2004): 016608, https://doi.org/10.1103/PhysRevE.70.016608.

## Supporting Information

Additional supporting information can be found online in the Supporting Information section.

**Supporting File**: smll76283-sup-0001-SuppMat.pdf.



16136829, 0, Downloaded from https://onlinelibrary.wiley.com/doi/10.1002/smll.76283 by JEREMY BAUMBERG - Cambridge University Library , Wiley Online Library on [16/10/2026]. See the Terms and Conditions (https://onlinelibrary.wiley.com/terms-and-conditions) on Wiley Online Library for rules of use; OA articles are governed by the applicable Creative Commons License